Check for updates

Synergetic effect between non-metals and dual metal catalysts for nitrogen reduction reaction†

Ji Zhang,[a] Weisong Yang[b] and Chenghua Sun [ID] *[c]

Nitrogen reduction reaction (NRR) is an essential process for ammonia synthesis. Currently, such process is overwhelmingly catalyzed with iron-based metal catalysts and still confronts the big challenge of high overpotential when room-temperature electrosynthesis is targeted due to the intrinsic inertness of N≡N bond in N_2. In this study, dual metal catalysts have been computationally designed and modulated by different non-metals dispersed in a graphene frame. As scanned by density functional theory (DFT) calculations, five candidates, namely $Fe_2@SN_4$, $Fe_2@BN_4$, $Co_2@BN_4$, $Co_2@PN_4$ and $Ni_2@PN_4$ catalysts, have been identified as promising catalysts with a calculated onset potential of −0.20, −0.27, −0.36, −0.34, and −0.33 V, respectively; more importantly, the competitive hydrogen evolution reaction (HER) can be well suppressed during the NRR. Such excellent catalytic performance origins from two synergetic effects, including the metal–metal and metal–ligands (non-metals) interactions, both of which can promote the electron transfer from d-orbitals of metal atom pair to the anti-bonding orbitals of adsorbed N_2 molecules. This can effectively activate the N≡N bond, resulting in low NRR onset potential and high NH_3 selectivity. The presented theoretical effort advances the theoretical understanding and provides guidance for the rational design of advanced non-precious NRR catalysts with high efficiency and selectivity.

Introduction

NH_3 plays an important role in numerous industrial production processes and human life owing to it being the main component of nitrogen fertilizers,[1] basic raw material for most industrial chemicals,[2] and an excellent green energy carrier.[3] The Haber–Bosch process (HBP), established more than 100 years ago, is still the dominating technology for large-scale ammonia production. However, this process requires high temperature (350–550 °C) and pressure (15–25 MPa)[4] to break the inert N≡N bond, under which condition a large amount of fossil energy is consumed along with severe emission of greenhouse gases. In this situation, extensive efforts have been made to search for environmentally friendly and resource-sustainable NH_3 synthesis methods.

Inspired by legumes effectively capturing N_2 from the atmosphere under ambient conditions, researchers have explored many strategies for the artificial fixation of N_2 to NH_3, including heterogeneous, photo, and electrical catalysis.[5–8] In particular, electrochemical nitrogen reduction reaction (NRR) is a promising alternative owing to its low cost, greenness, and easy accessibility.[9–11] Although numerous NRR catalysts have been reported, various open challenges, such as high overpotentials, poor selectivity, the consumption of precious metals, and low efficiency, make it far from achieving the performance of HBP,[12] which subsequently put forward a challenge to develop advanced electrocatalysts.

Single-atom catalysts (SACs) have been widely used in catalytic reactions owing to their unique electronic properties, ultrahigh utilization, and high catalytic activity and selectivity.[13–17] For the fabrication of SACs, two-dimensional materials have been widely used as the substrate to fix single metals, such as metal anchored in N-doped graphene to form M@Nx catalysts (M, N, and x represent the metal atom, nitrogen atom, and the number of N atoms, respectively), as demonstrated in various electrocatalytic reactions.[18–20] However, these catalysts feature a single active site, which often cannot meet the demand of these reactions with multiple elementary steps because the ideal reactivity requested by the early stage is often different or even opposite of the late stage. For instance, strong N–metal interaction is helpful to activate N_2, which is critical for its initial reduction, but such strong bonding often leads to difficult desorption of ammonia products at the late stage.[21–25]

As inspired by molecular catalysts,[26–28] several transition metals, such as Fe, Co, and Ni, are often active for NRR, whose

[a]Department of Electronical Engineering, Tongling University, Tongling, 244061, China
[b]Department of Communication and Electronics, Jiangxi Science and Technology Normal University, Nanchang, 330013, China
[c]Department of Chemistry and Biotechnology, Swinburne University of Technology, Hawthorn, VIC 3122, Australia. E-mail: chenghuasun@swin.edu.au
†Electronic supplementary information (ESI) available. See DOI: https://doi.org/10.1039/d3qi00517h

4746 | *Inorg. Chem. Front.*, 2023, **10**, 4746–4753

This journal is © the Partner Organisations 2023

empty d-orbitals can accept lone-pair electrons of N_2 to enhance the binding strength and donate the partially filled d-electrons back to the anti-bonding orbital of the molecular N_2 adsorbed on it to weaken the $N\equiv N$ triple bond.[29] As determined by this mechanism, transition metals need to be partially oxidized rather than pure metals or highly oxidized, as well demonstrated by Li et al.[30] This underlines the significant roles of surrounding ligands, which should offer a strong capacity to fix SACs, but cannot be too strong to fully oxidize active metals. Another key factor is conductivity, which is critically important for electron transport during electrocatalysis processes but hardly available when transition metals are fully oxidized. Therefore, a delicate balance has to be satisfied between strong fixation and proper metal–ligands interaction, which is an open challenge for the rational design of SACs. To overcome this issue, dual-metal catalysts, which feature metal–metal and multiple metal–ligands interactions, have been developed and demonstrated for NRR. Different from SACs, dual-metals offer the flexibility to choose large sets of metal combinations and work together, under which single metal–N interaction does not have to be strong;[31] more importantly, metal–metal bonding can offer excellent conductivity, as requested by NRR electrocatalysis. It is particularly worth noting that non-metals themselves can also serve as active center to catalyze NRR.[32] Such a strategy has been successfully demonstrated by dual-atom catalysts (DACs)[33,34] and even triple-atom catalysts.[35,36] Not surprisingly, the central question is what metal combinations are ideal.

In the present work, a computational effort has been made towards a systematic investigation of various combinations of dual metals using nonmetal-doped graphene as the substrate. Our design starts from low-cost elements for both transition metals and ligands, focusing on Fe, Co, and Ni as identified from early SACs studies.[37] Five nonmetals, including B, N, O, S, and P, have been scanned with N as the major one because N-doped graphene has been successfully synthesized and widely used to load SACs and DACs. Following these rules, dual metals are generated using five ligands, including 15 combinations with a formula $M_2@XN_4$ (M = Fe, Co, Ni; X = B, O, S, P, N). As demonstrated below, candidates have been identified as promising catalysts, namely, $Fe_2@SN_4$ (0.20 V), $Fe_2@BN_4$ (0.27 V), $Co_2@BN_4$ (0.36 V), $Co_2@PN_4$ (0.34 V), and $Ni_2@PN_4$ (0.33 V), with NRR onset potentials presented in the brackets, which outperform most of the current NRR catalysts.

Computational details

All the geometric optimization and energetic calculations were performed within the density functional theory (DFT) framework by employing the Vienna ab initio simulation package (VASP).[38] The exchange–correlation interactions were treated by the spin-polarized general gradient approximation (GGA) using the Perdew–Burke–Emzerhof functional.[39] The projector augmented wave (PAW) was used to describe the electron-ion interactions.[40] The plane wave energy cutoff of 400 eV and the

Monkhorst–Pack grid of $2 \times 2 \times 1$ k-point were set for structure relaxation, while the density of states (DOS) calculation was carried out by using a $4 \times 4 \times 1$ Monkhorst–Pack grid. The energy convergence criterion of 1×10^{-5} eV and maximum force of 0.02 eV $Å^{-1}$ were adopted to allow for full structural optimization. Bader charge analysis was applied to analyze the atomic charge and charge transfer.[41] To describe the van der Waals (vdW) interactions, the DFT-D3 (the semi-empirical dispersion-corrected density functional theory with the zero-damping method of Grimme) approach was used in the calculation.[42] The projected crystal orbital Hamilton population (pCOHP) was employed to analyze the intermediate orbitals and bond structure by using lobster code.[43,44] All structures obtained by DFT were visualized using the VESTA program.[45]

To evaluate the electrode potentials of the NRR process, the Gibbs free energies of intermediates were calculated using the computational hydrogen electrode (CHE) model introduced by Nørskov and co-workers.[46] In this study, the standard hydrogen electrode (SHE) was used as the reference electrode: $H^+ + e^- \rightarrow \frac{1}{2}H_2$ in equilibrium at 298.15 K and at 1 bar.

Thus, the free energy of proton/electron (H^+ and e^-) was set to the chemical potential of $\frac{1}{2}H_2$ under potential, $U = 0$, and pH = 0. In addition, all reactions were performed at 1 bar and 298.15 K.

The Gibbs free energy change for each reaction step is defined by the expression:

$$\Delta G = \Delta E + \Delta ZPE - T\Delta S + \Delta G_u + \Delta G_{pH} \tag{1}$$

where ΔE is the energy obtained from DFT calculation, ΔZPE is the change of zero point energy of the reactants and products obtained from the vibrational frequencies, and ΔS is the change of the entropy. The values of ΔZPE and $T\Delta S$ for each intermediate are listed in ESI.† ΔG_u represents the free energy change due to the electrode potential effect. $\Delta G_{pH} = k_B T \times \ln 10 \times pH$, where k_B is the Boltzmann constant and pH = 0 for the acid medium.

In the present study, transition metal pairs were anchored into a 5×5 supercell graphene containing three vacancies surrounded by five pyridinic N sites to form $M_2@NN_4$ (M = Fe, Co, Ni) structures, as shown in Fig. 1. If one N atom was substituted by another non-metal atom, such as B, O, S and P atoms, the $M_2@BN_4$, $M_2@ON_4$, $M_2@SN_4$, $M_2@PN_4$ structures were formed, respectively. These structures can be expressed uniformly by the formula $M_2@XN_4$ (M = Fe, Co, Ni; X = B, N, O, S, P). The vacuum layer was set to 20 Å to avoid interaction with the mirror image of slab. To evaluate the stability of paired metal atom catalysts, the average binding energy (E_b) was calculated as follows:

$$E_b = \frac{2E_M + E_{slab} - E_{M+M+slab}}{2} \tag{2}$$

where $E_{M+M+slab}$ denotes the energy of the surface embedded with two metal atoms, E_{slab} represents the energy of the non-metal element-doped graphene slab, and E_M is the energy of the single metal atom in a vacuum. Based on eqn (2), the more positive the binding energy is, the more stable the system.

This journal is © the Partner Organisations 2023

Inorg. Chem. Front., 2023, **10**, 4746–4753 | **4747**
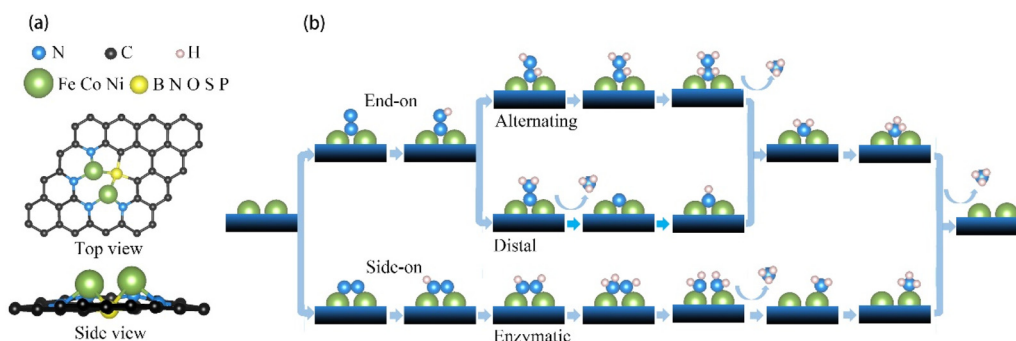
Fig. 1 Dual-atom catalyst (DAC) atomic model and the mechanism for nitrogen reduction reaction (NRR). (a) Transition metal atom pair anchored to the defective graphene matrix with four nitrogen atoms and another nonmetallic atom as its ligands. (b) Schematic representation of alternating, distal, and enzymatic mechanisms for NRR.

The intrinsic activity of an electrocatalyst is determined by the potential determination step (PDS), which has the most positive Gibbs free energy change (G_{max}). Based on the PDS, the onset potential U_{onset} ($U_{onset} = -\Delta G_{max}/e$) is computed to evaluate the catalytic performance, which is defined as the reducing potential with all steps in the pathway being thermodynamically downhill.

Results and discussion

To investigate the electrocatalytic properties of these DACs, we fully considered the possible mechanisms, which have been well-established and widely used over time as presented in Fig. 1b. As the first step of NRR, the molecular N_2 is adsorbed on the active sites to form an $*N_2$ intermediate through two configurations: end-on or side-on configuration, which then lead to three different hydrogenation pathways, including the distal or alternating reaction pathway for end-on configuration and enzymatic pathway for side-on configuration. Taking $Fe_2@SN_4$ as an example, we demonstrate the optimized structures of every intermediate for NRR along the three reaction pathways with both configurations, as shown in Fig. 2.

Two end-on geometries have been considered for initial N_2 adsorption, with N_2 adsorbed on the bridge site of Fe dimer and on the top site on one of the Fe atoms, with the former being energetically favorable, as shown in Fig. 2(a). With respect to free gas, following N_2 adsorption, the N–N distance increases from 1.09 Å to 1.17 Å due to the activation. The first proton–electron pair attacks the distal N to form $*NNH$ intermediate, which is the first step of six elementary reduction steps. Starting from the second hydrogenation, the reaction takes two different pathways, namely distal and alternating mechanisms. The $*NNH_2$ intermediates in the distal pathway still maintain adsorption on the bridge-site, but the $*NHNH$ intermediates in the alternating pathway transform into adsorption on the top-site, as fully demonstrated in Fig. 2(a). Different from distal/alternating paths, the enzymatic process starts from side-on adsorption, as shown in Fig. 2(b), with N_2

being fixed over two metals. With respect to end-on adsorption, the N–N distance is enlarged to 1.22 Å, indicating stronger activation of the N≡N bond, as shown in Fig. S1.† Following this adsorption, the full enzymatic pathway has been presented in Fig. 2(b), whose energy profiles will be further calculated.

To screen the optimal reaction pathway and catalysts, we calculated the free energy changes ΔG of PDS of each catalytic mechanism and then obtained the maximum change (ΔG_{max}) and the onset potential (U_{onset}), which can help us to compare the performance of different catalysts. The maximum change in free energy of 15 dual-atom catalysts for NRR *via* alternating, distal, and enzymatic pathways is summarized in Fig. 3. Except for $Fe_2@PN_4$, $Co_2@PN_4$, $Ni_2@NN_4$ and $Ni_2@SN_4$, the minimum ΔG_{max} appears at enzymatic pathways of all the DACs, indicating that the NRR on DACs prefers to take the enzymatic mechanism. This catalytic property may be ascribed to the synergetic effect of two transition metal atoms as active sites, which also occur in the natural N_2 fixation through the enzyme nitrogenase in diazotrophic micro-organisms[47] and other dual-site catalysts.[48,49] Furthermore, it should be noted that seven out of fifteen DACs exhibit excellent catalytic activity possessing very low values of $\Delta G_{max} < 0.40$ eV, including $Fe_2@BN_4$ (0.27 eV), $Fe_2@SN_4$ (0.20 eV), $Co_2@BN_4$ (0.36 eV), $Co_2@SN_4$ (0.30 eV), $Co_2@PN_4$ (0.34 eV), $Ni_2@ON_4$ (0.39 eV), and $Ni_2@PN_4$ (0.33 eV) catalysts, with ΔG_{max} being presented in the brackets.

For further performance evaluation of catalyst candidates, it is necessary to consider the competition between NRR and HER (hydrogen evolution reaction) that consumes protons and electrons. We investigated the HER process by calculating free energy change for the formation of $*H$, as shown in Fig. S2,† and then obtained the onset potentials for HER, which are compared with the corresponding onset potential for NRR, as illustrated in Fig. 4(a). As we can see that NRR is dominant in the bottom right region, while HER is dominant in the top left region. Five candidates, $Fe_2@BN_4$, $Fe_2@SN_4$, $Co_2@BN_4$, $Co_2@PN_4$, and $Ni_2@PN_4$, demonstrate both high catalytic selectivity and low onset potential for NRR, making them very promising candidates for the reduction of N_2.

4748 | *Inorg. Chem. Front.*, 2023, **10**, 4746–4753

This journal is © the Partner Organisations 2023
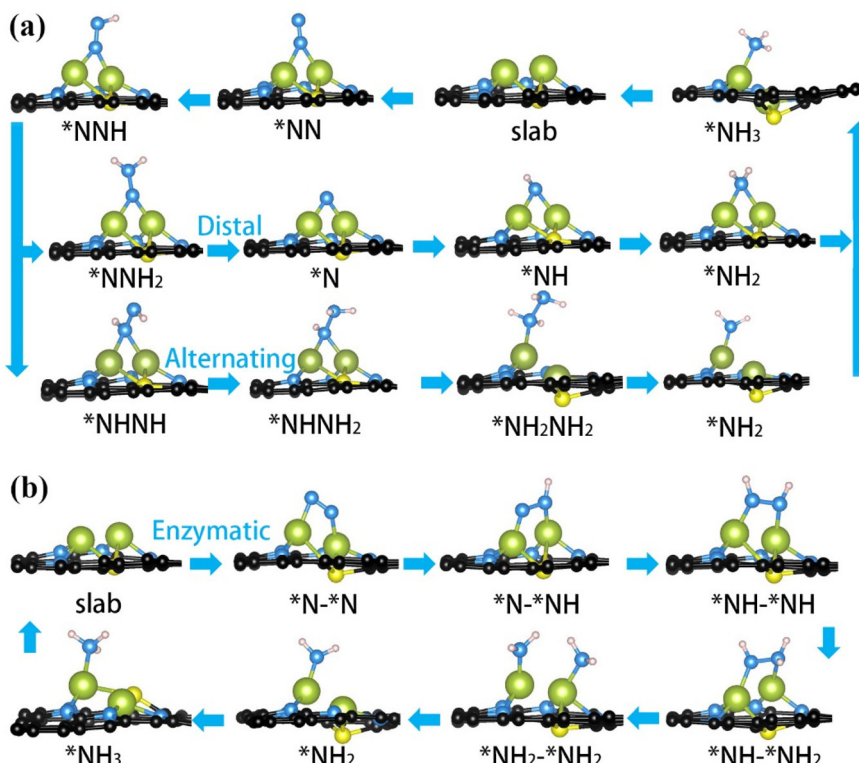
Fig. 2 Optimized structures of every intermediate adsorbed on Fe$_2$@SN$_4$ surface for NRR along distal and alternating pathways with (a) end-on configuration and enzymatic pathway with (b) side-on configuration.
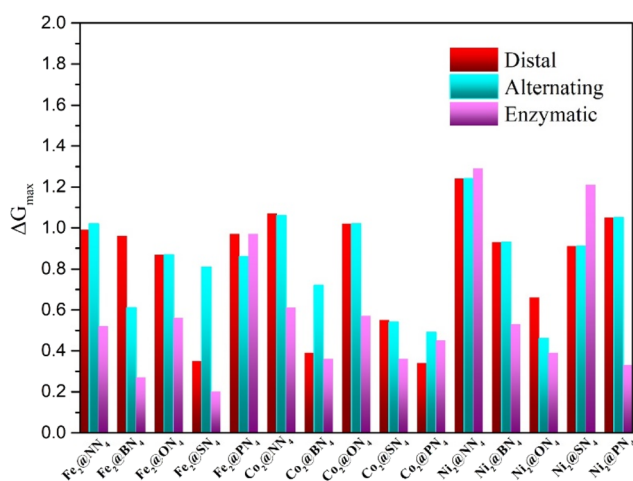

Fig. 3 Summary of the maximum change in free energy of 15 Dual-atom catalysts for NRR via alternating, distal, and enzymatic pathways.

The energetic details for NRR on five candidates are illustrated in free energy diagrams, as shown in Fig. 4(b)–(f). Accordingly, the adsorption free energy changes of N$_2$ molecule on Fe$_2$@SN$_4$, Co$_2$@BN$_4$, and Co$_2$@PN$_4$ catalysts are negative with values of −0.82 eV, −0.25 eV, and −0.37 eV, respectively, indicating that N$_2$ adsorption can occur spontaneously. Therefore, these catalysts are superior for the adsorption of N$_2$

to Fe$_2$@BN$_4$ and Ni$_2$@PN$_4$, which undergo 0.08 and 0.13 eV uphill, respectively. Additionally, for Fe$_2$@SN$_4$, Ni$_2$@PN$_4$, Co$_2$@BN$_4$, and Fe$_2$@BN$_4$, the PDS appears at the first proton–electron transfer step, while for Fe$_2$@BN$_4$, the PDS is found at the fifth step but not the first hydrogenation step. For the other DACs, the PDS is found almost at the first hydrogenation step, as seen in Table S2.† The PDS is directly related to the onset potentials, under which all the reaction steps are downhill. Especially, the Fe$_2$@SN$_4$ exhibits excellent catalytic activity with ultralow onset potential −0.20 V, which is less than that for the other Fe-based catalysts, such as FeN$_4$@Gra SAC (−1.66 V),[50] Fe$_2$N$_6$@Gra (−0.46 V) DAC,[49] and Fe(0001) flat surface (about −1.23 V).[51] It is worth mentioning that we also calculated the catalytic properties of the corresponding Fe@SN$_4$ SAC, which consists of a unitary single Fe atom as an active site, as shown in Fig. S1 and S3.† By contrast, the onset potential of Fe@SN$_4$ increases to −1.01 and −0.91 V through distal and enzymatic processes, respectively. Therefore, the improvement of catalytic performance may be attributed to both the synergistic effect of dual-metal active sites and significant boosting from proper ligands.

The origin of the high catalytic performance of DACs was further investigated by studying their electronic properties. First, the adsorption of N$_2$ molecules on the active site plays an important role, which is mainly related to orbital hybridization and electron transfer. As shown in Fig. 5(a), charge density differences for end-on and side-on adsorptions have

This journal is © the Partner Organisations 2023

Inorg. Chem. Front., 2023, **10**, 4746–4753 | **4749**
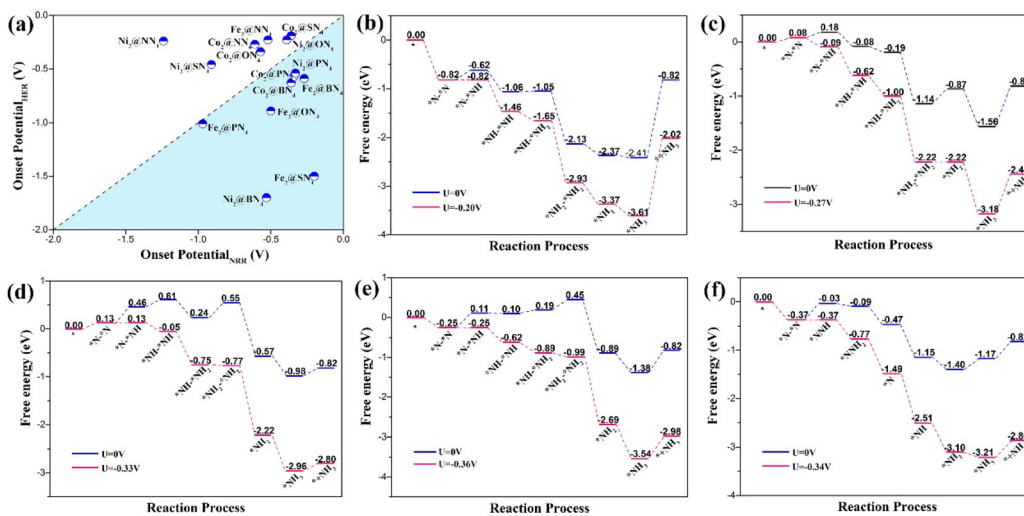
Fig. 4 NRR and HER selective analysis. (a) Computation of the onset potential of 15 TM paired-atom catalysts for NRR and HER. NRR is dominant in the bottom right region, while HER is dominant in the top left region. The calculated free energy profiles for NRR through the enzymatic mechanism on (b) $Fe_2@SN_4$ (c) $Fe_2@BN_4$ (d) $Ni_2@PN_4$ (e) $Co_2@BN_4$ and distal mechanism on (f) $Co_2@PN_4$.
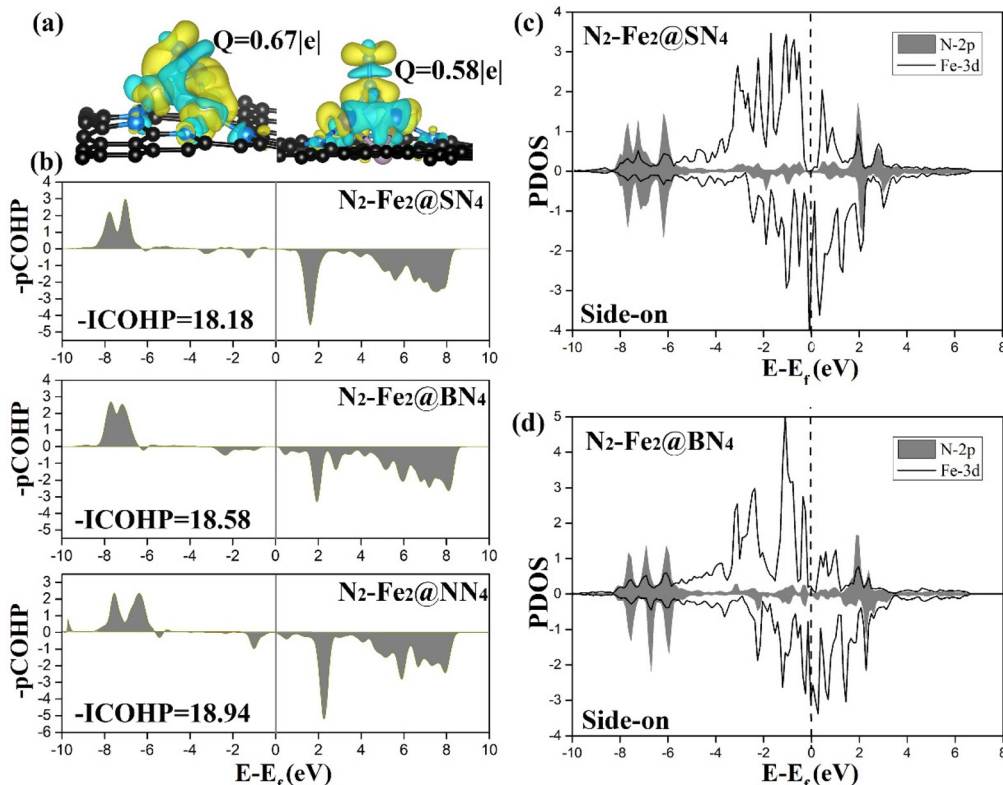

Fig. 5 Mechanism study of N_2 activation. (a) Charge density differences diagrams of $Fe_2@SN_4$ with N_2 adsorption with side-on and end-on configuration (the charge density accumulation and depletion areas are displayed in yellow and cyan); (b) projected crystal orbital Hamilton populations (pCOHP) for the N–N bonded to the $Fe_2@SN_4$, (c) $Fe_2@BN_4$, and $Fe_2@NN_4$ with side-on configuration, respectively, and (c) and (d) PDOS after N_2 adsorbed on the $Fe_2@SN_4$, $Fe_2@BN_4$, respectively (the d orbital of the Fe atom pair is shown by black line, and the N-2p orbital is represented by gray areas).

been presented, in which significant electron transfer has been observed from two metal centers. Given that bonding orbitals have been fully occupied in free N_2 gas, newly injected electrons from the catalysts will inevitably fill into the anti-bonding states; as a result, N_2 has been activated. To better understand the orbital interaction associated with N_2 acti-

4750 | *Inorg. Chem. Front.*, 2023, **10**, 4746–4753

This journal is © the Partner Organisations 2023

vation, projected crystal orbital Hamilton populations (pCOHP) and its integration (ICOHP) have been obtained for N–N adsorbed over Fe_2@SN_4, Fe_2@BN_4, and Fe_2@NN_4 with side-on configuration, as shown in Fig. 5(b). Interestingly, –ICOHP decreases slightly from 18.94 for Fe_2@NN_4 to 18.58 for Fe_2@BN_4 and 18.12 for Fe_2@SN_4. Such a result is essentially determined by the electronegativity; as a result, B and S, with Pauli electronegativity χ = 2.06 and 2.58,[52] present lower capacity to oxidize Fe dimer than that by N-ligands (χ = 3.04), which is helpful to keep the metal nature of Fe–Fe dimer. Such features can be better illustrated by calculated DOS profiles in Fig. 5(c) and (d). As demonstrated by calculated projected DOS of N-2p and Fe-3d orbitals after N_2 adsorption on Fe_2@SN_4, and Fe_2@BN_4 surfaces, two features can be summarized: (i) clear overlap area between the Fe-3d and N-2p has been observed, suggesting substantial orbital hybridization, which contributes to the electron transfer between N_2 adsorbate and DACs and is beneficial for N_2 activation; and (ii) stronger peaks at Fermi energy have been observed, as determined by lowly oxidized Fe_2. Towards efficient NRR, lone-pair electrons from N_2 fill into empty d-orbitals of partially oxidized transition metals, driving initial N_2 adsorption, following which metals further back donate electrons to the anti-bonding state of N_2 and result in effective activation. As illustrated in Fig. 5(a), the electron density accumulation areas are mainly observed between the Fe atom and N_2, indicating the enhancement of the N–Fe bond as a result of the electron transfer. In comparison, electron density depletion is mainly concentrated on the areas between adsorbed N atoms, which will activate the N≡N bond. Such analysis has been supported by Bader charge analysis, which shows an electron transfer of 0.67e from Fe_2 to N_2 adsorbed *via* side-on configuration. In contrast, the transferred electron to N_2 adsorbed *via* end-on configuration is only 0.58e, indicating that the adsorption of N_2 with side-on configuration is more conducive to the activation of N_2. As a reference, the transferred electrons to N_2 bound to single Fe@SN_4 is only 0.33e, as illustrated in Table S3,† indicating that the dual-metal atom site can significantly strengthen the electron donation to absorbed N_2 and subsequently enhance the catalytic activity. It is also worth noting that the transferred electrons are different from Fe dimer to N_2 adsorbed on the catalyst with different no-metal ligands, as illustrated in Table S3.† In particular, 0.57e transfer from Fe dimer to N_2 adsorbed on Fe_2@NN_4 catalyst. But the transferred electrons increase when another no-metal atom is introduced in ligands, which are related to the Pauli electronegativity of different no-metal elements.

Finally, the average binding energy E_b of the TM pairs was calculated to evaluate the stability of the M_2@XN_4 catalysts, which are listed in Table S3.† The binding energies for Fe_2@SN_4, Fe_2@BN_4, Co_2@BN_4, Co_2@PN_4, and Ni_2@PN_4 are calculated and compared with the cohesive energy associated with bulk metals in vacuum (bulk metal), 3.03(1.94), 5.46 (4.36), 5.76(3.09), 5.36(2.69) and 5.51(1.39) eV, respectively. The binding energies are all positive, indicating the metal pairs are thermodynamically stable in the non-metal doped

graphene. It is worth mentioning that dual-metal catalysts have been synthesized readily in experiments, such as isolated diatomic metal–nitrogen catalyst NiFe–N–C by a metal–organic framework (MOF) assisted method,[53] CoFe–N–C catalyst by a two-step pyrolysis process,[54] and ZnCo bimetallic sites supported on N doped carbon through a competitive complexation strategy.[55] The strategy to combine metal and non-metal ligands has been experimentally demonstrated by Zhao *et al.* with Fe–S–C linkage, showing impressive NRR performance.[56] Following these lab-based achievements, it is believed that the M_2@XN_4 catalysts proposed in this work are approachable experimentally.

Conclusions

In summary, we proposed the concept of dual-atom catalysts M_2@XN_4 for NRR, specifically using low-cost transition metals (Fe, Co, Ni) and non-metal ligands (O, S, P, B, N). High performance catalysts have been identified from computational scanning, with five outstanding candidates, Fe_2@SN_4, Fe_2@BN_4, Co_2@BN_4, Co_2@PN_4, and Ni_2@PN_4 catalysts, offering an onset potential as low as −0.20, −0.27, −0.36, −0.34, and −0.33 V. This is not only remarkably better than corresponding SACs, but also superior to expensive noble metals (such as single Ru[57]). These promising candidates also present excellent NRR selectivity over HER and catalyst stability. The electronic structure analysis displayed that the chemical environment around the metal atom-pair seriously impacts the electron transfer between adsorbed N_2 and catalysts, which plays an important role in the catalytic activity for NRR. We believe that our theoretical study on transition metal atom-pair catalysts provides guidance for the rational design of non-precious NRR catalysts with high efficiency and selectivity.

Conflicts of interest

There are no conflicts to declare.

Acknowledgements

References

1 Q. Wang, G. Zheng, S. Hao, X. Liu, J. Zheng, Y. Wang, Z. Su, N. Xu, Y. He, L. Lei and X. Zhang, Au_1Co_1 Alloy supported on graphene oxide with enhanced performance for ambient electrolysis of nitrogen to ammonia computational detail, *ACS Sustainable Chem. Eng.*, 2020, **8**, 44–49.

2 V. Rosca, M. Duca, M. T. de Groot and M. T. M. Koper, Nitrogen cycle electrocatalysis, *Chem. Rev.*, 2009, **109**, 2209–2244.

This journal is © the Partner Organisations 2023

Inorg. Chem. Front., 2023, **10**, 4746–4753 | **4751**

3 M. Aziz, T. Oda, A. Morihara and T. Kashiwagi, Combined nitrogen production, ammonia synthesis, and power generation for efficient hydrogen storage, *Energy Procedia*, 2017, **143**, 674–479.

4 M. Kitano, Y. Inoue, Y. Yamazaki, F. Hayashi, S. Kanbara, S. Matsuishi, T. Yokoyama, S. W. Kim, M. Hara and H. Hosono, Ammonia synthesis using a stable electride as an electron donor and reversible hydrogen store, *Nat. Chem.*, 2012, **4**, 934–940.

5 Y. Kobayashi, Y. Tang, T. Kageyama, H. Yamashita, N. Masuda, S. Hosokawa and H. Kageyama, Titanium-based hydrides as heterogeneous catalysts for ammonia synthesis, *J. Am. Chem. Soc.*, 2017, **139**, 18240–18246.

6 Z. Wang, W. Tian, Z. Dai, T. Zhou, Q. Mao, Y. Xu, X. Li, L. Wang and H. Wang, Bimetallic mesoporous RhRu film for electrocatalytic nitrogen reduction to ammonia, *Inorg. Chem. Front.*, 2021, **8**, 4276–4281.

7 X. Lu, M. Li, H. Wang and C. Wang, Advanced electrospun nanomaterials for highly efficient electrocatalysis, *Inorg. Chem. Front.*, 2019, **6**, 3012–3040.

8 X. Y. Cui, C. Tang and Q. Zhang, A review of electrocatalytic reduction of dinitrogen to ammonia under ambient conditions, *Adv. Energy Mater.*, 2018, **8**, 1800369.

9 J. Deng, J. A. Iñiguez and C. Liu, Electrocatalytic nitrogen reduction at low temperature, *Joule*, 2018, **2**, 846–856.

10 S. L. Foster, S. I. P. Bakovic, R. D. Duda, S. Maheshwari, R. D. Milton, S. D. Minteer, M. J. Janik, J. N. Renner and L. F. Greenlee, Catalysts for nitrogen reduction to ammonia, *Nat. Catal.*, 2018, **1**, 490–500.

11 G. Soloveichik, Electrochemical synthesis of ammonia as a potential alternative to the Haber-Bosch process, *Nat. Catal.*, 2019, **2**, 377–380.

12 A. R. Singh, B. A. Rohr, J. A. Schwalbe, M. Cargnello, K. Chan, T. F. Jaramillo, I. Chorkendorff and J. K. Nørskov, Electrochemical ammonia synthesis-the selectivity challenge, *ACS Catal.*, 2017, **7**, 706–709.

13 Y. J. Chen, S. F. Ji, C. Chen, Q. Peng, D. S. Wang and Y. D. Li, Single-atom catalysts: Synthetic strategies and electrochemical applications, *Joule*, 2018, **2**, 1242–1264.

14 Y. Pan, C. Zhang, Z. Liu, C. Chen and Y. D. Li, Structural regulation with atomic-level precision: From single-atomic site to diatomic and atomic interface catalysis, *Matter*, 2020, **2**, 78–110.

15 A. Q. Wang, J. Li and T. Zhang, Heterogeneous single-atom catalysis, *Nat. Rev. Chem.*, 2018, **2**, 65–81.

16 S. Sultan, J. N. Tiwari, A. N. Singh, S. Zhumagali, M. Ha, C. W. Myung, P. Thangavel and K. S. Kim, Single atoms and clusters based nanomaterials for hydrogen evolution, oxygen evolution reactions, and full water splitting, *Adv. Energy Mater.*, 2019, **9**, 1900624.

17 M. Ha, D. Y. Kim, M. Umer, V. Gladkikh, C. W. Myung and K. S. Kim, Tuning metal single atoms embedded in N x C y moieties toward high-performance electrocatalysis, *Energy Environ. Sci.*, 2021, **14**, 3455–3468.

18 H. Fei, J. Dong, D. Chen, T. Hu, X. Duan, I. Shakir, Y. Huang and X. Duan, Single atom electrocatalysts supported on graphene or graphene-like carbons, *Chem. Soc. Rev.*, 2019, **48**, 5207–5241.

19 X. Wan, X. Liu, Y. Li, R. Yu, L. Zheng, W. Yan, H. Wang, M. Xu and J. Shui, Fe–N–C electrocatalyst with dense active sites and efficient mass transport for high performance proton exchange membrane fuel cells, *Nat. Catal.*, 2019, **2**, 259–268.

20 H. T. Chung, D. A. Cullen, D. Higgins, B. T. Sneed, E. F. Holby, K. L. More and P. Zelenay, Direct atomic-level insight into the active sites of a high-performance PGMfree ORR catalyst, *Science*, 2017, **357**, 479–484.

21 C. He, Z. Y. Wu, L. Zhao, M. Ming, Y. Zhang, Y. Yi and J. S. Hu, Identification of FeN4 as an efficient active site for electrochemical N_2 reduction, *ACS Catal.*, 2019, **9**, 7311–7317.

22 F. Lü, S. Zhao, R. Guo, J. He, X. Peng, H. Bao, J. Fu, L. Han, G. Qi and J. Luo, Nitrogencoordinated single Fe sites for efficient electrocatalytic N_2 fixation in neutral media, *Nano Energy*, 2019, **61**, 420–427.

23 M. Zafari, M. Umer, A. S. Nissimagoudar, R. Anand, M. Ha, S. Umer, G. Lee and K. S. Kim, Unveiling the role of charge transfer in enhanced electrochemical nitrogen fixation at single-atom catalysts on BX sheets (X = As, P, Sb), *J. Phys. Chem. Lett.*, 2022, **13**, 4530–4537.

24 Y. Wan, H. Zhou, M. Zheng, Z. H. Huang, F. Kang, J. Li and R. Lv, Oxidation state modulation of bismuth for efficient electrocatalytic nitrogen reduction to ammonia, *Adv. Funct. Mater.*, 2021, **31**, 2100300.

25 M. Zafari, A. S. Nissimagoudar, M. Umer, G. Lee and K. S. Kim, First principles and machine learning based superior catalytic activities and selectivities for N 2 reduction in MBenes, defective 2D materials and 2D π-conjugated polymer-supported single atom catalysts, *J. Mater. Chem. A*, 2021, **9**, 9203–9213.

26 S. Shaw, D. Lukoyanov, K. Danyal, D. R. Dean, B. M. Hoffman and L. C. Seefeldt, Nitrite and hydroxylamine as nitrogenase substrates: mechanistic implications for the pathway of N_2 reduction, *J. Am. Chem. Soc.*, 2014, **136**, 12776–12783.

27 Y. Liu, S. Zhang, W. Li, H. Zhou, G. Wang and H. Zhang, Metal (Co/Mo)–N bond anchor-doped N in porous carbon for electrochemical nitrogen reduction, *Inorg. Chem. Front.*, 2021, **8**, 1476–1481.

28 T. J. Del Castillo, N. B. Thompson and J. C. Peters, A synthetic single-site Fe nitrogenase: high turnover, freeze-quench 57Fe Mössbauer data, and a hydride resting state, *J. Am. Chem. Soc.*, 2016, **138**, 5341–5350.

29 M. A. Légaré, G. Bélanger-Chabot, R. D. Dewhurst, E. Welz, I. Krummenacher, B. Engels and H. Braunschweig, Nitrogen fixation and reduction at boron, *Science*, 2018, **359**, 896–900.

30 Q. Li, S. Qiu, C. Liu, M. Liu, L. He, X. Zhang and C. Sun, Computational design of single-molybdenum catalysts for the nitrogen reduction reaction, *J. Phys. Chem. C*, 2019, **123**, 2347–2352.

4752 | *Inorg. Chem. Front.*, 2023, **10**, 4746–4753

This journal is © the Partner Organisations 2023

31 S. Gao, X. Liu, Z. Wang, Y. Lu, R. Sa, Q. Li, C. Sun, X. Chen and Z. Ma, Spin regulation for efficient electrocatalytic N$_2$ reduction over diatomic Fe-Mo catalyst, *J. Colloid Interface Sci.*, 2023, **630**, 215–223.

32 C. Liu, A. Tian, Q. Li, T. Wang, G. Qin, S. Li and C. Sun, Metal-Free Electrocatalysts for the Nitrogen Reduction Reaction, *EnergyChem*, 2023, **33**, 2210759.

33 L. J. Arachchige, Y. Xu, Z. Dai, X. Zhang, F. Wang and C. Sun, Theoretical investigation of single and double transition metals anchored on graphyne monolayer for nitrogen reduction reaction, *Phys. Chem. C*, 2020, **124**, 15295–15301.

34 L. J. Arachchige, Y. Xu, Z. Dai, X. Zhang, F. Wang and C. Sun, Double transition metal atoms anchored on Graphdiyne as promising catalyst for electrochemical nitrogen reduction reaction, *J. Mater. Sci. Technol.*, 2021, **77**, 244–251.

35 X. Wang, S. Qiu, J. Feng, Y. Tong, F. Zhou, Q. Li, L. Song, S. Chen, K. Wu, P. Su, S. Ye, F. Hou, S. Dou, H. Liu, G. Lu, C. Sun, J. Liu and J. Liang, Confined Fe-Cu clusters as sub-nanometer reactors for efficiently regulating the electrochemical nitrogen reduction reaction, *Adv. Mater.*, 2020, **32**, 2004382.

36 S. Gao, Z. Ma, C. Xiao, Z. Cui, W. Du, X. Sun, Q. Li, R. Sa and C. Sun, TM$_3$ (TM = V, Fe, Mo, W) single-cluster catalyst confined on porous BN for electrocatalytic nitrogen reduction, *J. Mater. Sci. Technol.*, 2022, **108**, 46–53.

37 T. Wang, Z. Guo, X. Zhang, Q. Li, A. Yu, C. Wu and C. Sun, Recent progress of iron-based electrocatalysts for nitrogen reduction reaction, *J. Mater. Sci. Technol.*, 2023, **140**, 121–134.

38 G. Kresse and J. Furthmüller, Efficient iterative schemes for ab initio total-energy calculations using a plane-wave basis set, *Phys. Rev. B: Condens. Matter Mater. Phys.*, 1996, **54**, 11169–11186.

39 J. P. Perdew, K. Burke and M. Ernzerhof, Generalized gradient approximation made simple, *Phys. Rev. Lett.*, 1996, **77**, 3865–3868.

40 P. E. Blöchl, Projector augmented-wave method, *Phys. Rev. B: Condens. Matter Mater. Phys.*, 1994, **50**, 17953–17979.

41 G. Henkelman, A. Arnaldsson and H. Jónsson, A fast and robust algorithm for Bader decomposition of charge density, *Comput. Mater. Sci.*, 2006, **36**, 354–360.

42 S. Grimme, J. Antony, S. Ehrlich and H. Krieg, A consistent and accurate ab initio parametrization of density functional dispersion correction (DFT-D) for the 94 elements H-Pu, *J. Chem. Phys.*, 2010, **132**, 154104.

43 R. Y. Rohling, I. C. Tranca, E. J. M. Hensen and E. A. Pidko, Correlations between density-based bond orders and orbital-based bond energies for chemical bonding analysis, *J. Phys. Chem. C*, 2019, **123**, 2843–2854.

44 S. Maintz, V. L. Deringer, A. L. Tchougreeff and R. Dronskowski, LOBSTER: A tool to extract chemical bonding from plane-wave based DFT, *J. Comput. Chem.*, 2016, **37**, 1030–1035.

45 K. Momma and F. Izumi, VESTA 3 for three-dimensional visualization of crystal, volumetric and morphology data, *J. Appl. Crystallogr.*, 2011, **44**, 1272–1276.

46 J. K. Nørskov, J. Rossmeisl, A. Logadottir, L. Lindqvist, J. R. Kitchin, T. Bligaard and H. Jonsson, Origin of the over-potential for oxygen reduction at a fuel-cell cathode, *J. Phys. Chem. B*, 2004, **108**, 17886–17892.

47 V. K. Shah and W. J. Brill, Isolation of an iron-molybdenum cofactor from nitrogenase, *Proc. Natl. Acad. Sci. U. S. A.*, 1977, **74**, 3249–3253.

48 T. He, A. R. P. Santiago and A. Du, Atomically embedded asymmetrical dual-metal dimers on N-doped graphene for ultra-efficient nitrogen reduction reaction, *J. Catal.*, 2020, **388**, 77–83.

49 T. Deng, C. Cen, H. Shen, S. Wang, J. Guo, S. Cai and M. Deng, Atom-Pair Catalysts Supported by N-Doped Graphene for the Nitrogen Reduction Reaction: d-Band Center-Based Descriptor, *J. Phys. Chem. Lett.*, 2020, **11**, 6320–6329.

50 J. Xie, H. Dong, X. Cao and Y. Li, Computational insights into nitrogen reduction reaction catalyzed by transition metal doped graphene: Comparative investigations, *Mater. Chem. Phys.*, 2020, **243**, 122622.

51 E. Skulason, T. Bligaard, S. Gudmundsdottir, F. Studt, J. Rossmeisl, F. Abild-Pedersen, T. Vegge, H. Jonsson and J. K. Norskov, A Theoretical Evaluation of Possible Transition Metal Electrocatalysts for N$_2$ Reduction, *Phys. Chem. Chem. Phys.*, 2012, **14**, 1235–1245.

52 J. Emsley, *The Elements*, Oxford University Press, 3rd edn, 1998.

53 W. Ren, X. Tan, W. Yang, C. Jia, S. Xu, K. Wang, S. C. Smith and C. Zhao, Isolated diatomic Ni-Fe metal-nitrogen sites for synergistic electroreduction of CO$_2$, *Angew. Chem., Int. Ed.*, 2019, **58**, 6972–6976.

54 X. Zhou, J. Gao, Y. Hu, Z. Jin, K. Hu and K. M. Reddy, Theoretically Revealed and Experimentally Demonstrated Synergistic Electronic Interaction of CoFe Dual-Metal Sites on N-doped Carbon for Boosting Both Oxygen Reduction and Evolution Reactions, *Nano Lett.*, 2022, **22**, 3392–3399.

55 Z. Lu, B. Wang, Y. Hu, W. Liu, Y. Zhao, R. Yang, Z. Li, J. Luo, B. Chi and Z. Jiang, An isolated zinc-cobalt atomic pair for highly active and durable oxygen reduction, *Angew. Chem.*, 2019, **131**, 2648–2652.

56 A. M. I. Ahmed, L. J. Arachchige, Z. Su, D. B. Hibbert, C. Sun and C. Zhao, Nitrogenase-Inspired Atomically Dispersed Fe–S–C Linkages for Improved Electrochemical Reduction of Dinitrogen to Ammonia, *ACS Catal.*, 2022, **12**, 1443–1451.

57 C. Liu, Q. Li, J. Zhang, Y. Jin, D. R. MacFarlanea and C. Sun, Conversion of dinitrogen to ammonia on Ru atoms supported on boron sheets: a DFT study, *J. Mater. Chem. A*, 2019, **7**, 4771–4776.

This journal is © the Partner Organisations 2023

Inorg. Chem. Front., 2023, **10**, 4746–4753 | **4753**